An analysis of the interaction between surface and basal crevasses in ice shelves

Maryam Zarrinderakht[1], Christian Schoof[1], and Anthony Peirce[2]

[1]Department of Earth, Ocean and Atmospheric Sciences, University of British Columbia, BC, Canada
[2]Department of Mathematics, University of British Columbia, BC, Canada

Correspondence: M. Zarrinderakht (mzaryam@eoas.ubc.ca)

Abstract. The prescription of a simple and robust parameterization for calving is one of the most significant open problems in ice sheet modelling. One common approach to modelling of crevasse propagation in calving in ice shelves has been to view crevasse growth as an example of linear elastic fracture mechanics. Prior work has however focused on highly idealized crack geometries, with a single fracture incised into a parallel-sided slab of ice. In this paper, we study how fractures growing

5   from opposite sides of such an ice slab interact with each other, focusing on different simple crack arrangements: we consider either perfectly aligned cracks, or periodic arrays of laterally offset cracks. We visualize the dynamics of crack growth using simple tools from dynamical systems theory, and find that aligned cracks tend to impede each other's growth due to the torques generated by normal stresses on the crack faces, while periodically offset facilitate simultaneous growth of bottom and top cracks. For periodic cracks, the presence of multiple cracks on one side of the ice slab however also generates torques that slow

10   crack growth, with widely spaced cracks favouring calving at lower extensional stresses than closely spaced cracks.

1 Introduction

Iceberg calving is a key process in the dynamics of marine ice sheets, since it regulates the length of floating ice shelves and consequently the rate at which ice is discharged across the grounding line (Schoof et al., 2017; Haseloff and Sergienko, 2018). Although there are numerous distinct approaches to model calving (e.g. Bassis and Ma, 2015; Benn et al., 2017; Cook et al.,

15   2014; Fastook and Schmidt, 1982; Nick et al., 2010, 2013; Nye, 1955; Todd and Christoffersen, 2014), there is currently no widely-accepted "universal calving law" that can be applied in large scale ice sheet and glacier flow models.

    Calving generally happens as the result of cracks growing to occupy the full thickness and width of an ice shelf. One common approach to model such cracks is to consider ice as elastic medium on the short time scales associated with fracture propagation, and to employ either a classical linear elastic fracture mechanics approach (Weertman, 1973, 1980; van der Veen,

20   1998a,b; Lai et al., 2020; Zarrinderakht et al., 2022), or to treat crack propagation as the result of breaking discrete bonds (Bassis, 2011; Aström et al., 2013; Crawford et al., 2021). The former leads to continuum models that identify the strength of stress singularities at crack tips as controlling whether a crack will propagate or not (Zehnder, 2012), and the computation of these "stress intensity factors" can be quite elaborate. In practice, this has restricted the use of linear elastic fracture to simple ice geometries with a single crack (Weertman, 1973, 1980; van der Veen, 1998a,b; Lai et al., 2020; Zarrinderakht et al., 2022),

25 for which interpolated Green's functions can be used to predict fracture propagation (Tada et al., 2000). This approach allows simple calving laws to be derived (Lai et al., 2020; Zarrinderakht et al., 2022) but leaves many open questions, such as whether crevasses incised into the bottom and top of the ice will typically grow simultaneously and meet in the middle to cause calving (as is implicitly assumed in some simpler calving models (e.g. Nick et al., 2010)), whether there is a preferred spacing between crevasses, and how the presence of multiple crevasses affects the calving laws constructed in Lai et al. (2020) and Zarrinderakht

30 et al. (2022).

Discrete element models (Bassis, 2011; Aström et al., 2013; Crawford et al., 2021) are better able to cope with multiple interacting cracks, and with cracks of arbitrary geometry, but they are computationally expensive and therefore difficult to apply when exploring larger regions of parameter space. It is also unclear exactly how their results depend on the exact geometry and density of bonds, the latter being edges in the network of discrete masses connected by springs that is used to describe the ice

35 mass in question. Nature provides no guide as to the bond network that should be most realistic (except possibly if the network is formulated at the scale of individual ice crystals, which is computationally impossible).

Here we attempt to bridge the gap between idealized classical fracture mechanics models and more complicated (and computationally much more expensive) discrete element models by extending prior work on linear elastic fracture mechanics models to take account of multiple interacting cracks. We use the boundary element method described in Zarrinderakht et al. (2022),

40 which can in principle handle arbitrary domain and crack geometries, to solve for stress intensity factors at crack tips and solve for their propagation. To keep the scope of our work tractable, we restrict ourselves to understanding simple interactions between basal and surface crevasses. In particular, we seek to identify how the spacing and alignment of crevasses on opposite sides of an ice shelf affect calving.

The paper is structured as follows: in section 4.3.1, we sketch the model presented by Zarrinderakht et al. (2022) and extend

45 it to accommodate the concurrent growth of multiple cracks. We show that the simultaneous propagation of two cracks can be cast as a two-dimensional semi-smooth dynamical system in terms of the two crack lengths and a minimal set of dimensionless parameters. We adopt the same weakly inertial crack propagation criterion used in Zarrinderakht et al. (2022). We assume that the total stress field is composed of an elastic stress induced by the newly introduced cracks, and a viscous pre-stress, and impose contact constraints that prevent opposite crack faces from penetrating into each other. In section 3.4.1, we describe how

50 crack propagation and the eventual steady state configuration that is attained from given initial conditions can be visualized using a phase plane. In section 3.4.2, we explore how changes in parameters affect those steady state configurations and ultimately leads to calving. Having focus initially on two aligned cracks in a wide domain, we find that such cracks naturally inhibit each other's growth. We therefore explore a periodic configuration with laterally offset cracks in section 3.4.3, finding qualitatively different behaviour in which calving due to growth of both crevasses is more prevalent. The results obtained from

55 a periodic domain are however sensitive to domain width, and we explore the effect of lateral crack spacing in section 3.4. We discuss implications of our results in section 3.5.

2 Model

The basic model is described in Zarrinderakht et al. (2022). In a Cartesian coordinate system $(x_1, x_2) = (x, z)$ where $z = 0$ is at sea level, we consider a parallel-sided slab of ice between $z = s$ and $z = b$, s being surface elevation and b basal elevation. The ice slab is assumed to be part of a larger ice shelf afloat in the ocean, so $s = (1 - \rho_i/\rho_w)H$ and $b = -(\rho_i/\rho_w)H$, where H is the thickness of the ice, and ρ_i and ρ_w are the densities of ice and water, respectively. We model only the portion of the slab of ice between $x = 0$ and $x = W$. The ice is subject to a viscous pre-stress of the form

$$\sigma_{11}^v = \rho_i g(s - z) + R_{xx}, \qquad \sigma_{22}^v = \rho_i g(s - z), \qquad \sigma_{12}^v = \sigma_{21}^v = 0, \tag{1}$$

where g is the acceleration due to gravity, and we consider the short-term elastic response (on time scales much less than a single Maxwell time) to the introduction of cracks into the lower and upper boundaries of the slab of ice. That elastic response takes the form of elastic stress that is added to the viscous pre-stress, and the high-stress concentrations at the tip of the cracks can cause the cracks to propagate.

As in Zarrinderakht et al. (2022), we prescribe a fluid pressure on the domain boundary: any part of the lower boundary below sea level is subject to hydrostatic water pressure in the ocean, while at the upper boundary, we prescribe a surface water level at

$$z = s - h_w. \tag{2}$$

Any part of the upper surface below that elevation is also subject to a hydrostatically increasing water pressure. We apply the same contact-type boundary conditions on crack faces as described in Zarrinderakht et al. (2022), meaning that normal compressive stress either attains the prescribed water (or atmospheric) pressure and the crack faces have moved apart, or normal compressive stress is at or above that fluid pressure, and the crack faces are touching. Other parts of the surface simply experience normal stress equal to the external fluid pressure, while shear stresses are assumed to vanish everywhere on the external boundary.

At the lateral domain boundaries at $x = 0$ and $x = W$, we apply either the same conditions of vanishing elastic shear and normal stress as in Zarrinderakht et al. (2022), or we apply periodic boundary conditions on elastic displacement and stress: in the notation of Zarrinderakht et al. (2022), the latter corresponds to

$$u_i(0, z, t) = u_i(W, z, t), \qquad \text{and} \qquad \sigma_{i1}^e(0, z, t) = \sigma_{i1}^e(W, z, t), \tag{3}$$

where u_i is the displacement field, σ_{ij}^e is the elastic stress as defined in Zarrinderakht et al. (2022), and i runs over $\{1, 2\}$.

We have previously considered only a single surface or basal crack in Zarrinderakht et al. (2022), in line with van der Veen (1998a,b) and Lai et al. (2020). Our goal in the present paper is to understand better how cracks interact with each other, focusing on the interaction between basal and surface cracks. To generalize our previous work but still retain enough simplicity to allow for qualitative insight, we consider one basal and one surface crack in the domain, of lengths d_t and d_b, respectively, and assume that both are oriented vertically; to the symmetry conditions we impose on their locations below makes that choice of orientation self-consistent.

The elastostatic problem of Zarrinderakht et al. (2022) allows us to compute a stress intensity factor K_{It} and K_{Ib} at the
90 tip of the surface and basal cracks, respectively, given the current domain geometry as well as material properties and forcing
parameters. As in Zarrinderakht et al. (2022), we assume that each crack propagates at a rate related to how much the stress
intensity factor exceeds fracture toughness K_{Ic} by Freund (1990),

$$\dot{d}_{\mathrm{b}} = \max\left(\frac{K_{\mathrm{Ib}} - K_{\mathrm{Ic}}}{K_{\mathrm{Ic}}|K'(0)|}, 0\right), \qquad \dot{d}_{\mathrm{t}} = \max\left(\frac{K_{\mathrm{It}} - K_{\mathrm{Ic}}}{K_{\mathrm{Ic}}|K'(0)|}, 0\right), \tag{4}$$

where the overdot indicates differentiation with respect to time, and $|K'(0)|$ is a constant related to Freund's (1990) universal
95 function. As discussed in Zarrinderakht et al. (2022), there are alternative hydrofracture-based models for crack tip propagation
that could replace this description, which we pursue here due to the qualitative insights it provides.

For a given position of the cracks along the domain, the domain geometry is fully specified by ice thickness H, domain
width W, and the crack lengths d_{t} and d_{b}. In other words, we can treat the right-hand sides in equations (4) as being functions
of d_{t} and d_{b}, and we obtain a set of two coupled first-order differential equations. All that the complicated elastostatic problem
100 described in Zarrinderakht et al. (2022) really does is to provide a means of computing K_{Ib} and K_{It} as functions of the dynamic
variables d_{t} and d_{b}.

In that vein, we will treat equations (4) as a two-dimensional dynamical system for $(d_{\mathrm{t}}, d_{\mathrm{b}})$. As in Zarrinderakht et al. (2022),
our interest will be in steady state crack configurations, in identifying which sets of initial conditions lead to which final crack
configurations, and in the effect of changing forcing and geometrical parameters on steady states and their basins of attraction.
105 In particular, we want to identify what changes in parameter values lead to the disappearance of steady states in which the ice
slab is only partially fractured so that cracks are either forced to propagate all the way across the ice or meet inside the ice. In
either case, we will interpret the result as calving: the detachment of one side of the domain from the other.

To simplify the set of geometrical and forcing parameters, we non-dimensionalize the model using the same set of scales as
in Zarrinderakht et al. (2022). This leaves only the following dimensionless parameters,

$$110 \quad \tau = \frac{R_{xx}}{\rho_{\mathrm{i}} g H}, \qquad \eta = \frac{h_w}{H}, \qquad \kappa = \frac{K_{Ic}}{\rho_{\mathrm{i}} g H^{3/2}}, \qquad W^* = \frac{W}{H}, \tag{5}$$

in addition to the dimensionless material constants given by

$$r = \frac{\rho_{\mathrm{i}}}{\rho_{\mathrm{w}}}. \tag{6}$$

Above, τ is a dimensionless extensional stress, η a dimensionless depth to the surface water table, and κ a dimensionless frac-
ture toughness. Using the Green's function formulation in Crouch and Starfield (1983), it can be shown that the solution for
115 stress in the model in Zarrinderakht et al. (2022) is independent of ν (while displacements do depend on Poisson's ratio). Con-
sequently, the dimensionless stress intensity factors K_{Ib}^* and K_{It}^* depend only on the scaled crack lengths and on (τ, η, W^*, r).
Equation (4) can therefore be written in the form

$$\dot{d}_{\mathrm{b}}^* = \max\left(K_{\mathrm{Ib}}^*(d_{\mathrm{b}}^*, d_{\mathrm{t}}^*; \tau, \eta, W^*, r) - \kappa, 0\right), \qquad \dot{d}_{\mathrm{t}}^* = \max\left(K_{\mathrm{It}}^*(d_{\mathrm{b}}^*, d_{\mathrm{t}}^*; \tau, \eta, W^*, r) - \kappa, 0\right), \tag{7}$$

where the asterisk decorations on the crack length variables and stress intensity factors denote their dimensionless counterparts,
120 scaled with ice thickness H and with with the stress intensity $\rho_{\mathrm{i}} g H^{3/2}$, respectively.
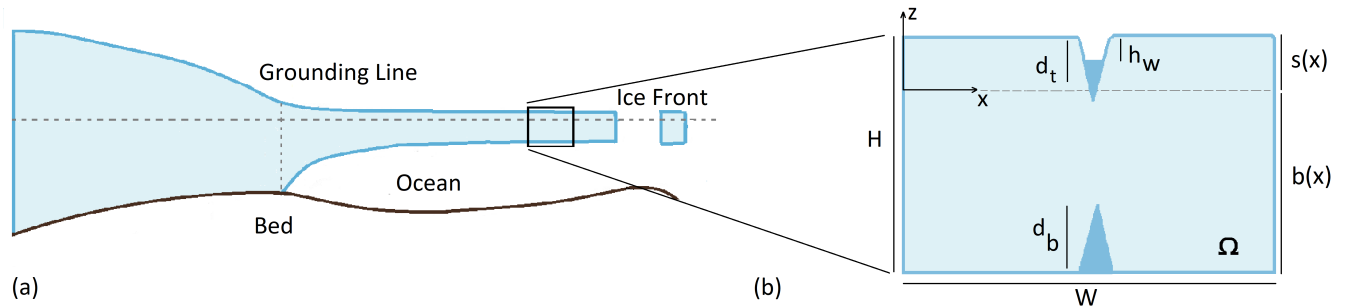
Figure 1. Geometry of the problem: the finite domain shown in panel (b) is intended to represent part of a floating ice shelf, with two aligned crevasses, one each at the upper and lower surfaces.

Note that, for simplicity, we immediately omit the asterisk decorations, in the understanding that all variables and parameters used below are dimensionless. Any changes in forcing parameters occur much more slowly than cracks propagate, so the dimensionless forcing and geometry parameters τ, η, κ, and W are constant during crack propagation. The problem at hand is therefore an autonomous two-dimensional dynamical system, and we rely primarily on phase planes to visualize the behavior of the system: in the $(d_\mathrm{b}, d_\mathrm{t})$-plane, we plot curves traced out by $d_\mathrm{t}(t)$ against $d_\mathrm{b}(t)$ as t increases for a solution to the dynamical system; these are the *orbits* of the dynamical system (7) (e.g. Strogatz, 1994). Plotting orbits on a phase plane provides a simple graphical way of identifying the behavior of the system for a given set of parameters, for all possible initial conditions. In practice, we use the boundary element method described in Zarrinderakht et al. (2022) to solve for the right-hand sides of (7) and use the MATLAB routine *streamslice* to generate phase planes.

3 Results

3.1 Phase planes for aligned cracks

First, we generalize the geometry considered in Zarrinderakht et al. (2022) by introducing aligned surface and basal cracks at the mid-way point $x = W/2$ as in figure 1. Note that the intention here is to mimic the infinitely wide domain of van der Veen (1998a,b) and Yao et al. (2004), and we use a large domain width $W = 10$, applying the same boundary conditions of vanishing elastic traction as Zarrinderakht et al. (2022).

Figure 2 shows an example of a $(d_\mathrm{b}, d_\mathrm{t})$-phase plane for this geometry. There are several non-standard qualitative features in this phase plane that turn out to be generic for the dynamical system (7), in each case related to the maximum over $K_\mathrm{I} - \kappa$ and zero taken on the right-hand side of equations (7). First, by construction, crack lengths can never shrink, so all orbits are either horizontal, vertical or angled upwards to the right: if a stress intensity factor is less than the fracture toughness, the corresponding crack tip simply does not move.

Second, the dynamical system is non-smooth: the maximum ensures not only ensures that cracks cannot shrink, it generally renders the system non-differentiable where $K_\mathrm{Ib}^* = \kappa$ or $K_\mathrm{Ib}^* = \kappa$, even if K_Ib and K_It are smooth functions of $(d_\mathrm{b}, d_\mathrm{t})$.
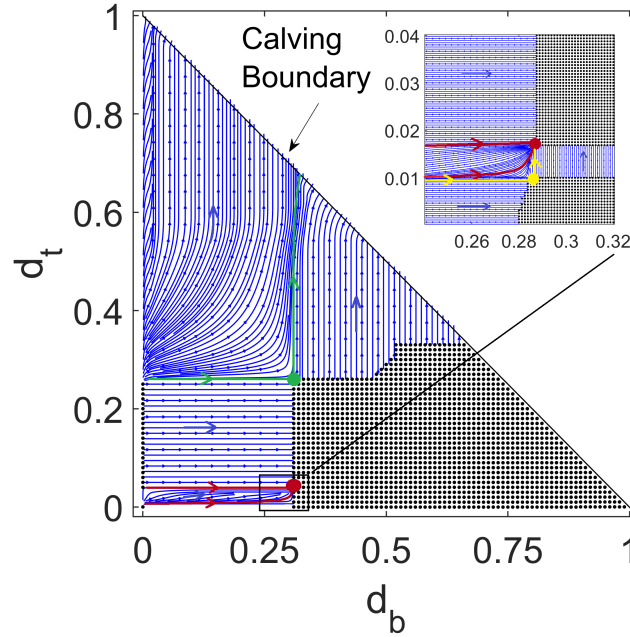
Figure 2. Phase plane diagram for two aligned cracks for $\tau = 0.02$, $\eta = 0.04$, $\kappa = 0.001$, $W = 10$ and $r = 0.89$. The inset shows an enlargement of the region marked as a black box around $x = 0.28$. Blue curves are orbits of the dynamical system (7), the direction in which (d_b, d_t) evolves in time is indicated by blue arrowheads. The region of black dots indicates steady-state solutions for which both stress intensity factors are less than fracture toughness κ. The coloured dots indicate saddle-type (green and yellow) and node-type (red) marginal fixed points as defined in the main text, while the green curve is the separatrix connection of the d_t-axis to the saddle-like green fixed point. A small region of steady states near the origin is not visible due to its small size, as is a thin strip of non-steady states close to the d_b-axis extending to the right of $d_b = 0.28$, discernible only in the inset.

For simplicity, we will refer to the sets of points for which $K_{\mathrm{Ib}}^* = \kappa$ or $K_{\mathrm{Ib}}^* = \kappa$ as marginal d_b- and d_t-nullclines, respectively: these are the curves along which one of the elastostatic stress intensity factors is equal to the fracture toughness. Some awkward terminology is necessary here because a nullcline is simply a set of points for which $\dot{d}_b = 0$ or $\dot{d}_t = 0$; for smooth dynamical systems, these sets are generally one-dimensional curves, which is not the case here as we describe below. The non-differentiability manifests itself visually in figure 2 through the boundary between regions in which the orbits are purely horizontal or vertical (so $K_{It}^* < \kappa$ or $K_{Ib}^* < \kappa$, respectively), and "curved" orbits, along with both crack lengths change simultaneously.

Third, equilibria of the dynamical system are generally not isolated but occupy regions of finite size, rendered with black dots in Figure 2. These regions are bounded by parts of the marginal nullclines defined above (where stress intensity factors are equal to the fracture toughness). Inside the regions of steady states, both stress intensity factors are less than the fracture toughness.

In addition, the phase plane here is bounded: crack lengths must be positive, and for aligned cracks, their sum must be less
than the ice thickness. When using dimensionless crack lengths scaled with H, the crack tips meet when

$$d_{\mathrm{b}} + d_{\mathrm{t}} = 1, \tag{8}$$

which we take to correspond to calving as marked in Figure 2.

The usual notions of phase plane analysis, like identifying isolated fixed points and their stability, do not apply without
modification due to the non-differentiability of the dynamical system, and due to the fact that equilibria occupy extended
regions of the phase plane. There are however two equilibria that occupy a special role here, namely those where two marginal
nullclines intersect. We will refer to these equilibria as marginal fixed points below. There are three such equilibria in Figure
2, although one is only visible in the enlargement in the inset.

One, marked with a red dot, is analogous to a stable node in standard phase plane analysis, and we will therefore refer to it
as a "stable node" in a slight abuse of terminology. If we start the system with small surface and basal cracks of length $d_t(0)$
and $d_b(0)$, they will evolve towards this equilibrium solution provided the ratio $d_t(0)/d_b(0)$ is large enough and $d_t(0)$ as well
as $d_b(0)$ are not too small. For the small values of κ relevant to typical ice shelves, there is a small region around the origin in
the phase plane (not visible in Figure 2 due to its small size) in which neither crack will grow. When we state that orbits started
near the origin will evolve towards the node, we have to add that they need to start outside that small region. The existence of
short steady-state crack lengths has been discussed previously (van der Veen, 1998a; Lai et al., 2020), and is associated with
low-stress intensity factors, scaling as $d^{1/2}\tau$ for the surface crack, and $d^{1/2}(\tau - 1 + r^{-1})$ for the basal crack (see appendix
C1 of Zarrinderakht et al., 2022): for small enough d, these are guaranteed to be less than fracture toughness κ. An analogous
region of very short steady-state cracks can be seen for instance in Figures 4 and 7 in Zarrinderakht et al. (2022).

Even though the stable node is not an attractor in the strict sense (there are other equilibria arbitrarily close to the stable
node), it does have a finite basin of attraction. The size of that basin of attraction is overstated by the main panel due to the
finite resolution used in computing the phase portrait. Close to the stable node is a marginal fixed point that is analogous to
a saddle in standard phase plane analysis, marked with a yellow dot in the inset. For this marginal fixed point, a single orbit
ends at the saddle, while a second orbit connects saddle and node. Below the orbit leading up to the saddle, there are additional
orbits starting with lower values of $d_t(0)/d_b(0)$ that terminate at the boundary of a region of steady states.

The third marginal fixed point is marked with a green dot in Figure 2 and plays the role of a saddle in a standard phase
plane. Here, the orbit that connects the d_t-axis to the saddle (analogous to a separatrix in a standard phase plane) divides initial
conditions that lead to immediate calving from initial conditions that lead to stable, steady cracks of finite length that leave the
ice slab intact.

3.2 Changes in crack configuration due to altered forcing

A phase plane helps visualize the behavior of the dynamical system for fixed parameter values and is analogous in that regard to
for instance to Figure 10 of van der Veen (1998a), or Figures 4 and 7 in Zarrinderakht et al. (2022) for the single-crack systems
considered in these papers. Suppose the system is started with only small seed cracks to initiate crevasse growth (where these

seed cracks need to be large enough in order to start outside the region of steady states around the origin discussed above). Calving will then occur if there is an orbit connecting the near-origin initial conditions in the phase plane to the calving boundary at $d_{\mathrm{b}} + d_{\mathrm{t}} = 1$. In Figure 2, that is not the case: instead, cracks will evolve to the configuration represented by the red dot, or one very close to it.

As in Zarrinderakht et al. (2022), we ask how the marginal fixed point at the red dot evolves under changes in forcing parameters, and how such changes can themselves lead to calving. The same caveat applies here as in our earlier work (see section 4.5 of Zarrinderakht et al. (2022)): in asking how the dynamical system changes under changes in parameters, and how an existing crack configuration is affected, we are ignoring the fact that the viscous pre-stress will generally not remain the of the same form as assumed in our model even over relatively short time scales (comparable with the Maxwell time of ice), and changes in domain geometry will occur as the result of viscous flow over long time scales so that results based on the rectangular geometry assumed here will eventually become misleading. We address these issues in the companion paper Zarrinderakht et al. (submitted).

In Figure 3, we plot phase planes analogous to Figure 2 for a range of values of η and τ as indicated for each column and row of the grid. Figure 2 is reproduced in panel c2. If we track the position of the stable node-type marginal fixed point in figure 2, we find that it moves upwards and to the right (that is, in the direction of flow of the dynamical system) under increases in extensional stress τ, while it remains unchanged under an increase in η (that is, an increase in the depth of the water table). In other words, if τ is increased, $(d_{\mathrm{b}}, d_{\mathrm{t}})$ will track the position of the node, but conversely, remain stranded in the region of steady states indicated by black dots under a subsequent reduction in τ. This is analogous to becoming stranded in the grey region of steady states in Figure 6 of Zarrinderakht et al. (2022). The insensitivity to η by contrast is easy to understand in terms of the shallow depth of the top crack d_{t} at the node: the tip of the surface crack is above the water level in columns 2–4 of Figure 3.

Calving under increases in τ eventually occurs for each of columns 2–4 through the node meeting the diagonal calving boundary in row a, with the surface crack length d_{t} remaining very shallow: calving occurs almost entirely by the propagation of the basal crack. The critical value of τ in each case lies somewhere between $\tau = 0.03$ and $\tau = 0.04$, which is consistent with the critical value of $\tau = 0.039$ for calving by basal crevasse propagation determined numerically in Zarrinderakht et al. (2022).

The saddle-type marginal fixed point moves downwards and to the right under increases in τ, and moves downwards under decreases in η. An alternative calving mechanism, starting with a stable steady state configuration like the node in panel c2, is to raise the surface water level (that is, to decrease η) until the two marginal fixed points annihilate each other: this is analogous to the saddle-node bifurcations of Figures 6a and 6b of Zarrinderakht et al. (2022) (for instance, by going from panel c2 to panel c1 in Figure 3 here). When that annihilation occurs due to a reduction in η, the length of the basal crack remains almost unchanged during the subsequent evolution of $(d_{\mathrm{b}}, d_{\mathrm{t}})$: the asymptote orbit emerging from the saddle is nearly vertical, and hence the motion in the phase plane from the equivalent of a saddle-node bifurcation is also nearly vertical. Calving driven by changes in water level occurs almost entirely by the propagation of the surface crack.

In fact, if we suppose that a step from one panel in Figure 3 to a neighboring panel corresponds to calving (for instance, starting from the node in c2 and changing parameter values to those in c1, or starting from the node in panel b2 and changing
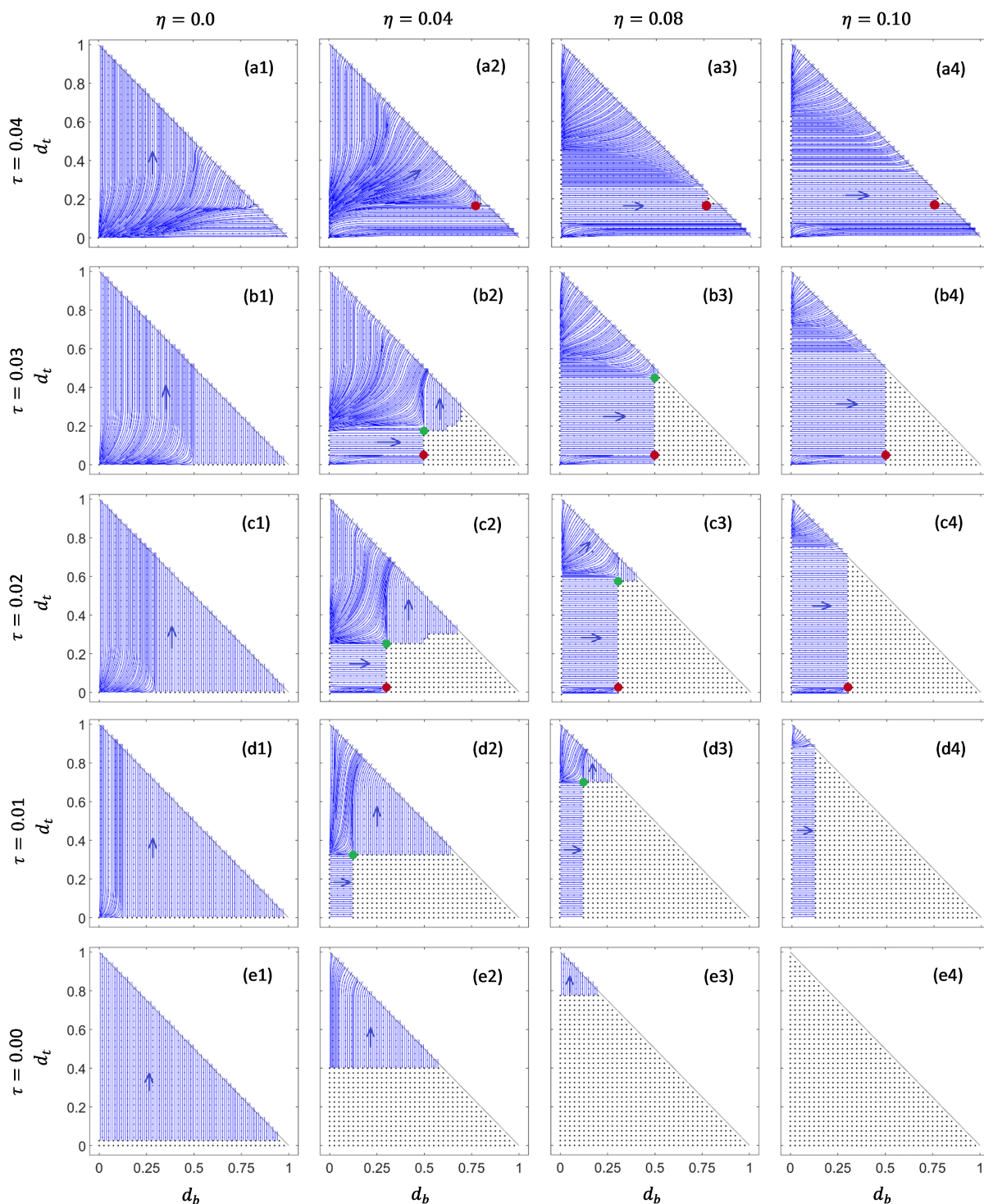
Figure 3. Gridded phase plane diagrams for two aligned cracks. $\eta =$ (0 (column 1), 0.04 (column 2), 0.08 (column 3), 0.1 (column 4) and $\tau = 0.04$ (row a), 0.03 (row b), 0.02 (row c), 0.01 (row d), 0 (row e).
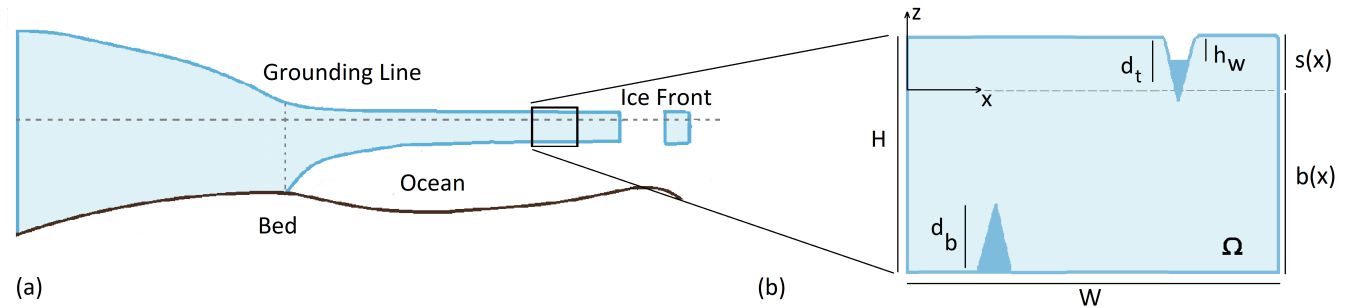
Figure 4. A periodic domain with offset cracks at $x = W/4$ and $x = 3W/4$.

parameter values to those in b1), then we can identify which crack will propagate to cause calving purely by looking at orbits that emerge near the origin in the panel in which calving occurs: in panel c1, orbits emerging near the origin evolve predominantly upward. More significantly still, if we start an orbit near the origin with $d_b = 0$, that orbit will evolve to the

225 calving boundary at $d_t = 1$ while maintaining zero basal crack length. Similarly, orbits emerging near the origin in panel b1 evolve predominantly to the right, and an orbit started near the origin with $d_t = 0$ will evolve to calving at $d_b = 1$ with zero surface crack length.

In other words, in order to predict parameter combinations that lead to calving with aligned cracks, we can actually look at the dynamics of surface and basal cracks in isolation: our admittedly coarse sampling of parameter space strongly suggests that

230 calving occurs from near the origin (a nearly unfractured initial domain) as from the node configuration (with a short surface and larger basal crack). One crack is always dominant, and the propagation of one crack does not significantly reinforce the propagation of the other.

A plausible physical explanation of this behavior is provided by the torques generated on each crack face (see also Zarrinder-akht et al., 2022, appendix C2): the torque generated by extensional stress on and fluid pressure in the bottom crack induces

235 a rotation on both sides of the crack (see also Figure 10 of Zarrinderakht et al. (2022)) that tends to compress the ice surface, and vice versa for the torque generated on a surface crack.

3.3 Offset crevasses in a periodic domain

Motivated by our conjecture that torques generated by a crack on one side of the domain affect the propagation of a crack incised into the opposite side of the ice, we consider whether the dynamics of misaligned (or laterally offset) cracks differ qualitatively

240 from those of aligned cracks: presumably, if a basal crack causes compression at the upper surface, that compression is strongest above the basal crack and decreases with horizontal distance.

To maintain the requisite symmetry for laterally offset cracks to act as mode I crack and propagate vertically, we assume that they are located at $x = W/4$ and $x = 3W/4$, and switch to laterally periodic boundary conditions as in equations (3): as a result, the model describes a periodic array of surface and bottom cracks, in which the surface and bottom cracks are spaced a

245 half-wavelength $W/2$ apart (Figure 4).

Figure 5 shows a grid of phase planes analogous to Figure 3. One obvious difference is that the "calving boundary" now consists of the lines $d_b = 1$ and $d_t = 1$: offset cracks will no longer meet part-way through the ice. We find similar behavior in Figure 5 as in Figure 3 for cases where crack evolution away from the origin does not lead to immediate calving, with a node-type marginal fixed point evident in panels d2–e2, c3–e3 and b4–e4. The corresponding saddle-type fixed point does not always exist, being absent in panels b4 and c4 (which is also the case in Figure 3, panels b4 and c4).

A subtle but significant qualitative difference with 3 is the size of the surface crack at the node point: while basal crack length d_b is significantly larger than surface crack length d_t, the latter is much bigger than in figure 3. As a consequence, the tip of the surface crack is above the water level in several of the examples in Figure 5, and the node point moves upwards as η is decreased in several examples (for instance, in going from panel 5c4 to panel 5c3, or panel 5d3 to panel 5d2.

This has a knock-on effect on the style of calving under increases in extensional stress: in the aligned crack case of Figure 3, an increase in extensional stress invariably leads to calving by basal crack propagation (see the discussion in section 3.2, and columns 2–4 of Figure 3). In the offset crack case of figure 5, increases in τ by contrast lead to calving by top crack propagation through the annihilation of saddle and node points (panels d2–c2, c3–b3) more frequently than by the node point reaching the right-hand calving boundary (panels b4–a4), while the annihilation of saddle and node points in a saddle-node bifurcation only occurs as the result of a decrease in η in Figure 3.

3.4 The effect of periodicity

The results in the previous section suggest that the presence of offset instead of aligned cracks may promote the simultaneous growth of both cracks: specifically, the motion of the node-type marginal fixed point under changes in parameter values involves significantly greater growth of the surface crack.

A second notable feature of Figure 5 as compared with Figure 3 is however that the values of extensional stress τ are significantly larger in the former than the latter, even though, qualitatively we obtain roughly similar phase planes (with a node and saddle type marginal fixed point in some of them, and therefore with parameter combinations that lead to finite crack growth but not to calving if starting near the origin). The fact that larger extensional stresses are required to produce a qualitatively similar result is not the result of having laterally offset versus aligned cracks, but of using a periodic domain with a relatively short ($W = 1$) length: in addition to surface and basal cracks interacting, neighboring cracks on each of the surfaces also interact.

Here we analyze the interaction between neighboring cracks, restricting ourselves to a periodic array of basal cracks for simplicity. The second equation in (7) then becomes redundant, and the dynamical can be visualized simply by plotting K_{Ib} against d_b, identifying where $K_{\mathrm{Ib}} > \kappa$. We show results in Figure 6. Panel a shows how K_{Ib} depends on crack length d_b for fixed a value of $W = 2$ as τ is varied, analogously to Figure 7b in Zarrinderakht et al. (2022). For a given set of parameters, the crack will grow if $K_{\mathrm{Ib}} > \kappa$ (the latter being the broken straight line), and remain static otherwise. Calving occurs if, as in the curves for $\tau = 0.12$ in Figure 6a, $K_{\mathrm{Ib}} > \kappa$ up to the limiting value $d_b = 1$, at which the basal crack fully penetrates through the ice thickness. As shown in Figure 6b, this is the case for larger τ, mimicking qualitatively the corresponding behavior for a non-periodic domain studied in Zarrinderakht et al. (2022).
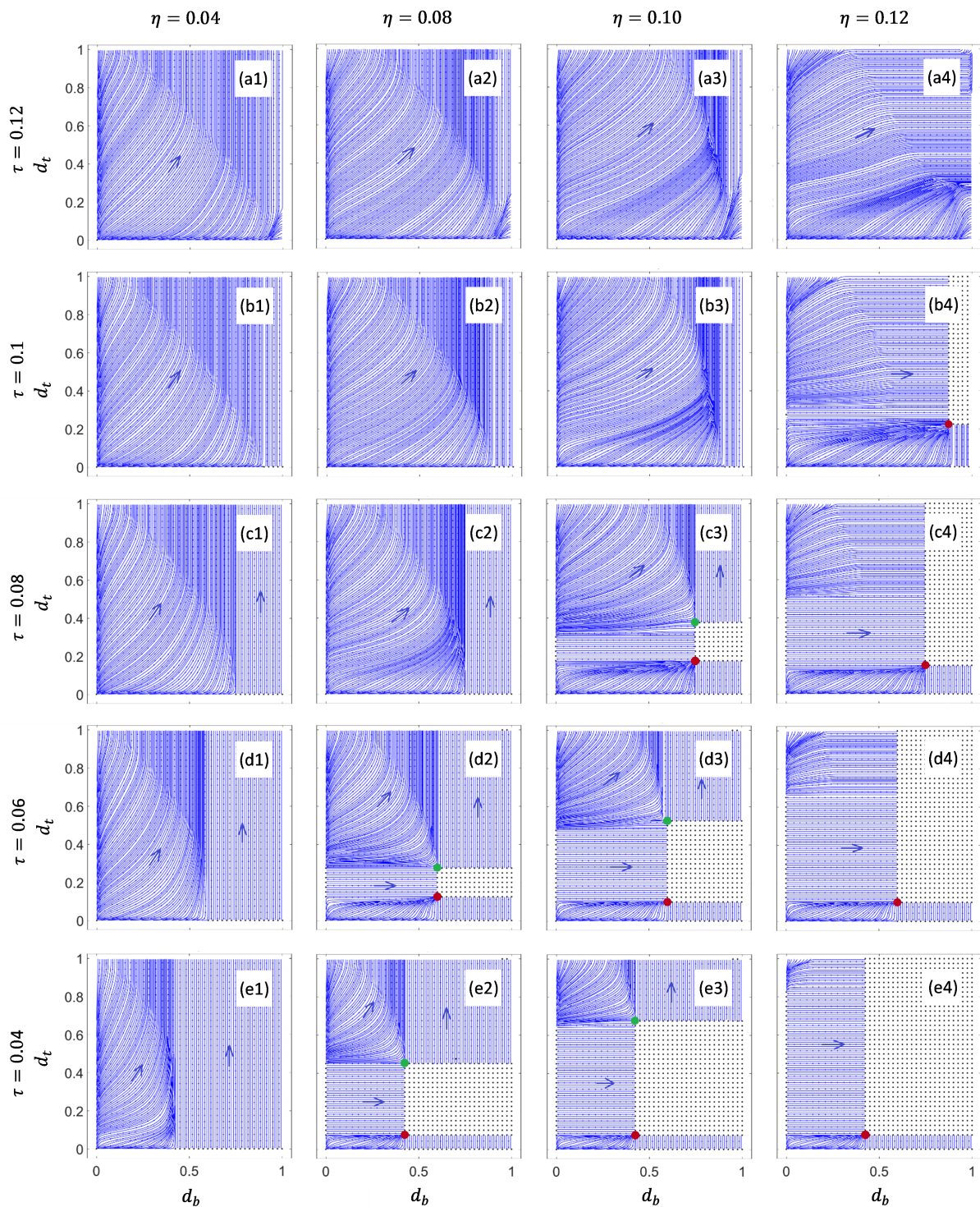
Figure 5. Gridded phase plane diagram for two offset cracks with periodic boundary conditions and $W = 1$, same plotting scheme as Figure 3. $\eta = 0.04$ (column 1), 0.08 (column 2), 0.1 (column 3), 0.12 (column 4), and $\tau = 0.12$ (row a) 0, 1 (row b), 0.8 (row c) 0.06 (row d) and 0.04 (row e).
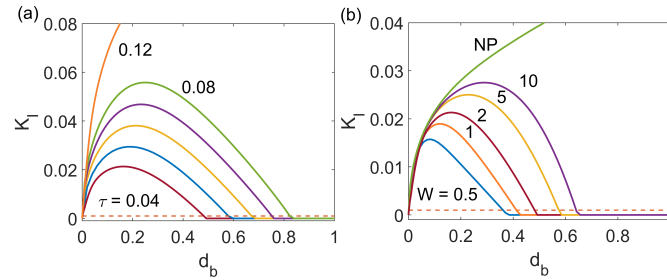
Figure 6. (a) Stress intensity factor K_{Ib} against crack length with $W = 2$ for a basal crack for different values of $\tau = 0.04$ (red), 0.05 (blue), 0.06 (yellow), 0.07 (purple), 0.08 (green) and 0.12 (orange). (b) Scaled stress intensity factor versus the crack length for different values of scaled periodic domain length, $W = 0.5$ (blue), 1 (orange), 2 (red), 5 (yellow), 10 (purple), and non-periodic domain shown by NP (green), for $\tau = 0.04$. The result for the non-periodic domain was computed for $W = 10$ but is insensitive to the domain width for traction-free lateral boundary conditions. The dashed horizontal line in both panels indicates the fixed parameter value $\kappa = 0.001$. The crack grows if $K_{\mathrm{Ib}} > \kappa$, and remains static otherwise.

Figure 6b similarly shows K_{Ib} against crack length for a fixed value of $\tau = 0.04$, just above the critical value of 0.039 for calving by basal crack propagation for a non-periodic domain in Zarrinderakht et al. (2022). The curve marked "NP" reproduces the corresponding result for that domain, given by the purple curve in Figure 7b of Zarrinderakht et al. (2022). If we compare the case of a finite-width periodic domain with the case of the non-periodic domain, we find that K_{Ib} agrees between the two for short crack lengths d_{b}, for which the far field is relatively unimportant. The difference becomes noticeable as d_{b} grows, more so for short periodicities W. Only the non-periodic case experiences calving at $\tau = 0.04$ in Figure 6b.

For each combination of parameters τ and κ and a given domain periodicity W, the points of intersection between the corresponding solid curve and the dashed curve in Figure 6 correspond to marginal equilibria as defined in section 3.1, with the smaller solution being unstable and the larger being stable if it exists. As extensional stress is increased, the larger, stable marginal equilibrium also increases, until it disappears entirely. Figure 7a shows the corresponding steady states for $W = 10$ as a continuous function of the parameter τ, by analogy with Figure 8b in Zarrinderakht et al. (2022). The grey region consists of steady states for $W = 10$ as an example.

Calving for basal cracks, therefore, occurs through the continuous growth of crevasse length with increasing τ until $d_{\mathrm{b}} = 1$ is reached at a critical value τ_{crit}. For the case $W = 10$ shown in Figure 6a, $\tau_{\mathrm{crit}} = 0.088$, as compared with $\tau_{\mathrm{crit}} = 0.039$ for a non-periodic domain. In figure 7b, we plot the dependence of τ_{crit} on W: the larger W, the lower the critical stress. We conjecture (but have not attempted to prove) that the limit of τ_{crit} for large W is given by the critical stress for a non-periodic domain with traction-free lateral boundaries, $\tau_{\mathrm{crit},\infty} = 0.039$. If so, the decrease in τ_{crit} clearly continues to be significant beyond the range for which we have calculated τ_{crit} in Figure 7: for $W = 20$, τ_{crit} is a little under twice of the critical value for a non-periodic domain.

As in the non-periodic case considered in Zarrinderakht et al. (2022), calving occurs because K_{Ib} changes from vanishing as $d_{\mathrm{b}} \to 1$ for $\tau < \tau_{\mathrm{crit}}$ to becoming infinite for $\tau > \tau_{\mathrm{crit}}$ (Figure 6a). In Zarrinderakht et al. (2022, appendix C), we were able to
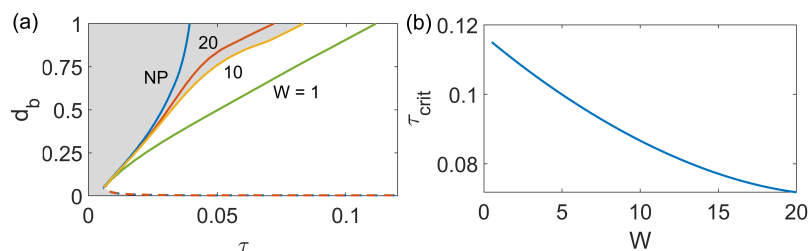
Figure 7. (a) Bifurcation diagram for a periodic domain with a single basal crack with $W = 1$ (green), 10 (yellow), 20 (red) and non-periodic domain shown by NP (blue). The region of steady states generally lies to the left of each curve, as indicated by grey shading for $W = 10$. (b) The critical extensional stress as a function of the domain width W.

associate that behavior with the net torque generated by the crack on the remaining "neck" of ice immediately above the crack. In a non-periodic domain with vanishing lateral traction, the torque generated by forces on the crack face must be balanced by a torque generated by stresses in the neck of ice. The balance of torques dominates the stress field in the neck when the crack spans nearly the full ice thickness, and a positive stress intensity factor (diverging to $+\infty$ as $d_\mathrm{b} \to 1$ results if the net torque on the crack remains positive for basal crack lengths approaching unity.

In the present case, the torque generated by one crack is balanced not only by the torque in the overlying neck of ice but also by torques due to all the other cracks in the periodic array, which reduces the torque and therefore stresses generated in the neck of ice. The smaller the spacing W between cracks, the stronger that effect becomes, which we can visualize by looking at the vertical displacement u_3 around the crack. Figure 8 shows the stress field σ_{xx} and corresponding deformation of the domain for identical parameter values $\tau = 0.1$.

Clearly, stresses are larger around the crack tip for the non-periodic case in panel a. Far-field displacements u_z displacement are also larger for the non-periodic case, and linear in x, without any applied traction at the lateral boundaries, the far field undergoes a rigid body motion. By contrast, the periodic case has smaller far-field displacement with a finite, negative curvature: far from the crack, the stress and displacement fields are those for an elastic beam, with the curvature signaling a bending moment that resists the torque generated in the crack.

4 Discussion

4.1 Towards a calving law

As in the simpler case of a single crack studied by van der Veen (1998a,b), Lai et al. (2020) and Zarrinderakht et al. (2022), we can attempt to create a calving law for the case of interacting cracks. Identifying which parameter combinations (τ, η, κ) result in calving given an initial state with only minimal crack lengths $(d_\mathrm{b}(0), d_\mathrm{t}(0))$ is relatively simple. First, the initial crack lengths need to be sufficient for the stress intensity factor to overcome the typically small fracture toughness κ. As the crack lengths are short, the effect of interactions between cracks is minimal in that case: the results of van der Veen (1998a,b), Lai
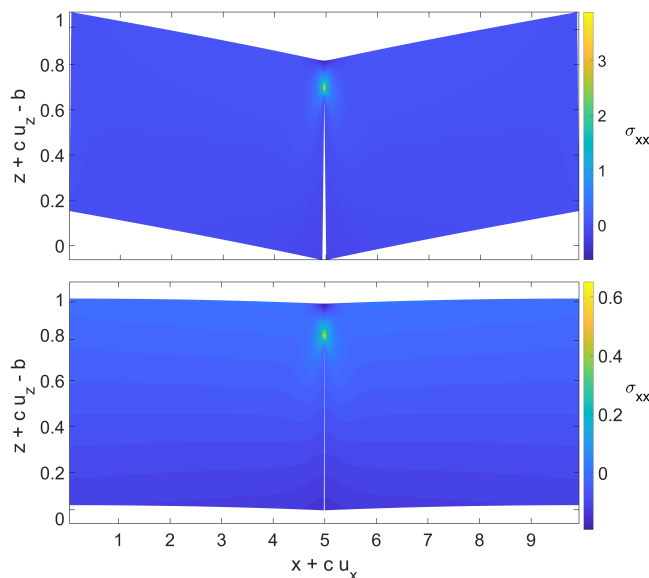
Figure 8. The stress distribution for a basal crevasse with $\tau = 0.1$ and $d_{\mathrm{b}} = 0.8$ for (a) a non-periodic domain with $W = 10$, (b) a periodic domain with $W = 10$. As in Figure 10 of Zarrinderakht et al. (2022), we illustrate the results here using a deformed domain, plotting σ_{xx} against Eulerian position $(x + cu_x, z + cu_z)$ with $c = 0.02$.

et al. (2020) and Zarrinderakht et al. (2022) suffice, with both Lai et al. (2020) and Zarrinderakht et al. (2022) furnishing the relevant criteria. Second, the ensuing crack propagation needs to result in the cracks either meeting inside the ice as in section

325 3.2, or one crack propagating fully through the ice as in section 3.3. That outcome is easy to identify through the absence of the node-type marginal fixed point in the relevant phase planes, as shown in Figure 3 and 5. The relevant region of parameter space can be delineated crudely from Figures 3 and 5 directly, which could be improved upon by identifying conditions under which the fixed point marginally exists (defining the boundary of the region of parameter space in which calving occurs): for instance, when it first appears at the "calving boundary" (the diagonal $d_{\mathrm{b}} + d_{\mathrm{t}} = 1$ in Figure 3, or the right-hand edge $d_{\mathrm{b}} = 1$

330 in Figure 5), or when it first forms at a saddle-node bifurcation (for instance, between the parameter values used in panels d2 and c2 of Figure 5).

A more complicated problem is the construction of a calving law that allows for slow changes in the forcing parameters: by slow, we mean as compared with the natural time scale of crack evolution in the dynamical system (7), which is likely the case in any realistic setting, where extensional stress τ and water level η typically evolve on the advective time scale for ice

335 transport across an ice shelf, and on the seasonal time scale associated with surface melt, respectively. In that situation, cracks may propagate only part-way across the ice. Calving can occur because of subsequent changes in forcing parameters to cause them to propagate further and eventually meet in the ice or reach the opposite ice surface.

In the confines of our model, the difference between calving by such slow changes in forcing parameters, and instant calving as discussed above is that the cracks will have a significant initial length at the instant that a critical parameter combination

permitting calving is reached. The analogous situation for a single crack was discussed in section 5 of Zarrinderakht et al. (2022) and led to a relatively simple prescription for calving (equation (37) of Zarrinderakht et al. (2022)), but the present case is more complex to capture.

Consider the case of offset cracks as shown in Figure 5. The simplest approximation is to assume that the region of steady states indicated by black dots as in panels d2–e2, c3–e3 and b4–e4 always takes the form of a rectangle with its sides aligned with the $(d_{\mathrm{b}}, d_{\mathrm{t}})$-axes. Let the upper and lower boundaries of the region be at $d_{\mathrm{tm}}^{+}(\tau, \eta, \kappa)$ and $d_{\mathrm{tm}}^{-}(\tau, \eta, \kappa)$, and the left-hand boundary at $d_{\mathrm{bm}}(\tau, \eta, \kappa)$. If any one of these boundaries is not present (as is the case for d_{tm}^{+} in panels b4 and c4), then simply set the corresponding value of $d_{\cdot\mathrm{m}}$ to unity.

The marginal node-type marginal fixed point, if present, must be at $(d_{\mathrm{tm}}^{-}, d_{\mathrm{bm}})$, and any initial evolution is to that fixed point, at least to a close approximation. Subsequent movement of the boundaries of the rectangle of steady states can have one of four consequences. First, the node can move upwards and to the right, and in which case the crack configuration $(d_{\mathrm{b}}, d_{\mathrm{t}})$ tracks the location of the node. Second, the node can move downwards and to the left, leaving the crack configuration $(d_{\mathrm{b}}, d_{\mathrm{t}})$ static and inside the region of steady states. Third, the node can move down and to the right, in which case d_{b} tracks the left-hand edge d_{bm} of the region of steady states, while d_{t} remains static. Forth, the node can move upwards and to the left, in which case d_{t} tracks the bottom of the region of the steady states at d_{tm}^{-} while d_{b} remains static.

Any movement of the boundaries of the region of steady states at d_{tm}^{+}, d_{tm}^{-}, and d_{bm} that occurs later leads to a similar pattern of crack evolution: $(d_{\mathrm{b}}, d_{\mathrm{t}})$ will either move horizontally to stay on the left-hand edge of the region of steady states, move vertically to stay on the bottom edge, move diagonally to track the corner that is the node-type marginal fixed point or remain inside the region of steady states if none of the other alternatives are possible. That is until either $(d_{\mathrm{b}}, d_{\mathrm{t}})$ reaches the right-hand edge of the unit square and calving occurs by the propagation of the bottom crack all the way to the upper ice surface, or the upper boundary of the region of steady states reaches the location $(d_{\mathrm{b}}, d_{\mathrm{t}})$. The latter outcome can occur either as a result of the upper boundary reaching a location $(d_{\mathrm{b}}, d_{\mathrm{t}})$ that had previously ended up on the inside of the region of steady states or because the upper boundary d_{tm}^{+} reaches the lower boundary at d_{tm}^{-} and the two marginal fixed points annihilate each other in a saddle-node bifurcation. In either event, calving occurs by the propagation of the surface crack to the base of the ice.

Mathematically, we can capture the implied motion of the phase point $(d_{\mathrm{b}}, d_{\mathrm{t}})$ under changes in parameter values by the following statement, analogous to equation (37) in Zarrinderakht et al. (2022): let

$$S_{\mathrm{b}}(\tau, \eta, \kappa) = \{d : d > d_{\mathrm{bm}}(\tau, \eta, \kappa)\}, \qquad S_{\mathrm{t}}(\tau, \eta\kappa) = \{d : d_{\mathrm{tm}}^{-}(\tau, \eta, \kappa) \leq d < d_{\mathrm{tm}}^{+}\} \cup \{1\}. \tag{9}$$

Then, if T is a slow time variable associated with the change in parameters (as opposed to the fast time variable with respect to which the dynamical system (7) evolves), then we can write

$$d_{\mathrm{b}}(T) = \inf\{d : d \in S_{\mathrm{b}}(\tau(T), \eta(T), \kappa(T) \,\text{and}\, d > d_{\mathrm{b}}(T') \,\text{for all}\, T' < T\}, \tag{10}$$

$$d_{\mathrm{t}}(T) = \inf\{d : d \in S_{\mathrm{t}}(\tau(T), \eta(T), \kappa(T) \,\text{and}\, d > d_{\mathrm{t}}(T') \,\text{for all}\, T' < T\}; \tag{11}$$

all that is then required is to know how the boundaries of the region of steady states depend on τ, η, and κ.

4.2 Limitations of the model

We have not attempted to complete the calculation suggested at the end of the last subsection, namely to compute in detail
how the boundary of the region of steady states depends on forcing parameters. The reason is that Figure 5 (on which the
375 procedure described was based) was computed for a specific value W of the spacing between crevasses, and we demonstrated
in section 3.4 that our results are highly sensitive to that spacing. More specifically, we found no preferred finite spacing
between crevasses at which calving occurs most easily (Figure 7b). It appears that basal crevasses propagate more easily the
further apart they are spaced, as the torques exerted on each other by neighboring cracks have the effect of acting to close
the tracks (Figure 8), and this makes the exercise of trying to define a calving rule for finitely-spaced crevasses an exercise of
380 limited value.

The absence of an optimal, finite crevasse spacing at which crack propagation occurs most easily (in the sense of calving
occurring at the lowest possible extensional stress τ) likely points to the same deficiency in the model as previously discussed
in section 6.3 of Zarrinderakht et al. (2022): based on the assumption of small-strain elasticity, the model neglects the effect
of vertical elastic displacements on fluid pressure at the domain boundary. In other words, the effect of elastic deformation on
385 buoyancy is excluded from the model, even though at large lateral distances, we can expect sufficient vertical displacements
to have a leading order effect. We anticipate that incorporating the feedback between displacement and fluid pressure at the
boundary will lead to additional torques generated by vertical displacements in the far field, suppressing crack growth for very
large crack spacings. We leave a study of this effect to future work.

In addition to not accounting for the effect of buoyancy on elastic stresses, a second limitation of the present model is its
390 insistence on a parallel-sided slab as the basic domain into which cracks are incised, and consequently the use of a viscous pre-
stress that corresponds to an unfractured, parallel-sided ice slab. In practice, we expect these assumptions to break down over
different time scales: first, once cracks have propagated to a steady state configuration in which they span only part of the ice
thickness, the elastic stress built up during fracture propagation will decay viscoelastically over a single Maxwell time, likely
on the order of hours in an ice shelf (Olinger et al., 2022). After that viscoelastic relaxation, the form of the pre-stress assumed
395 here as well as in van der Veen (1998a,b), Lai et al. (2020) and Zarrinderakht et al. (2022) will no longer be appropriate; a more
complicated recomputation of the viscous pre-stress on the now partially fractured domain becomes necessary (Krug et al.,
2014). Second, over the much longer time scale associated with significant viscous deformation of the ice shelf (typically
decades or longer), even the fractured ice domain will no longer take the form of a parallel-sided slab with narrow cracks
incised into them: the cracks will be widened by viscous flow, significantly altering the domain on which the linear elastic
400 fracture mechanics problem considered here needs to be solved. We consider both of these complications in the companion
paper (Zarrinderakht et al., submitted).

5 Conclusions

In this study, we modeled the simultaneous growth of both basal and surface crevasses which has received less attention in
the literature due to a lack of tabulated Green's functions. Here a semi-smooth two-dimensional dynamical system is used

405 to display crack growth rate, $(\dot{d}_b, \dot{d}_t)$, and their interactions as a phase plane with the constraints imposed by the contact conditions. The orbits in this system show the direction of propagation flows with arrows. In other words, it shows the rate of evolution of crack length as a function of the current crack length for a fixed set of parameters. The steady regions are shown by dots that no crack penetration occurs. This model can predict the evolution of cracks to either a steady state or to the point where the cracks span the width of the ice, known as calving, for a given set of initial conditions and parameters.

410 For two aligned crevasses in the shelf, we observed that the top crack dominates when the water level is high and there is a significant amount of water in it. When the shelf is intact, the basal crack grows rapidly and reaches a steady state where the hydrostatic pressure is equal to the cryostatic pressure. Meanwhile, the surface crack, despite containing a large amount of water, remains small and stable until a certain point and then becomes unstable and grows to span the entire thickness of the shelf. This study showed that no set of parameters can result in both cracks growing simultaneously from an undamaged

415 shelf to calving while considering only one crack is insufficient to cause calving. The model indicates that one crack is always dominant, and the scenario of two aligned cracks growing at the same time to a steady state is not predicted. This behavior can be attributed to the difference in crack growth speed and stress intensity factor at the crack tips. The results support the conclusion that the calving criteria established by Zarrinderakht et al. (2022) is effective for the case of two aligned crevasses and does not require any modification to the system behavior.

420 Driven by our hypothesis that torques produced by a crack on one side of the domain can impact a crack on the opposite side of the ice, we investigated laterally offset cracks. To ensure that misaligned cracks maintain the necessary symmetry to function as a mode I crack and propagate vertically, we assume that they are located at regular intervals. Considering periodic boundary conditions and the frequency of cracks on a shelf can improve stability and resistance to crack propagation under higher extensional stress. In this case, the domain length and crack spacing become effective, and as the domain grows and the

425 crack separation increases, the stress intensity factors also increase. The model proposed in this study, similar to Zarrinderakht et al. (2022), does not account for the buoyancy effect that generates a torque to stabilize the crack, resulting in a tilt in the domain. However, periodic boundary conditions counteract this bending effect by reproducing the crack pattern as the shelf bends back down to the next crack. In addition, applying periodic boundary conditions causes steady state and fixed points to occur at later stages of larger crack lengths.

430 *Code availability.* The code for calculations is available from the corresponding author upon request.

Author contributions. MZ executed the research. MZ and CS designed the project and wrote the paper. MZ and AP developed the numerical method and the code. All authors edited the paper.

Competing interests. The authors declare no competing interests

Acknowledgements. MZ was supported by the ArcTrain NSERC CREATE graduate training program and by NSERC Discovery Grant
435 funding to CS. CS acknowledges NSERC Discovery Grant RGPIN-2018-04665. AP acknowledges the support of NSERC Discovery Grant
RGPIN-2015-06039.

References

Aström, J., Riikilá, T., Tallinen, T., Z. T., Benn, D., Moore, J., and Timonen, J.: A Particle Based Simulation Model for Glacier Dynamics, The Cryosphere, 7, 1591–1602, 2013.

440 Bassis, J.: The Statistical Physics of Iceberg Calving and the Emergence of Universal Calving Laws, Journal of Glaciology, 57, 2011.

Bassis, J. and Ma, Y.: Evolution of Basal Crevasses Links Ice Shelf Stability to Ocean Forcing, Earth and Planetary Science Letters, 409, 203–211, 2015.

Benn, D., J., A., Zwinger, T., Todd, J., Nick, F., Cook, S., Hulton, N., R. J., and Luckman, A.: Melt-under-cutting and Buoyancy-driven Calving from Tidewater Glaciers: New Insights from Discrete Element and Continuum Model Simulations, Journal of Glaciology, 63,

445 691– 702, 2017.

Cook, S., Rutt, I. C., Murray, T., Luckman, A., Zwinger, T., Selmes, N., A., G., and James, T. D.: Modelling Environmental Influences on Calving at Helheim Glacier in Eastern Greenland, The Cryosphere, 8, 827–841, 2014.

Crawford, A., Benn, D., and Todd, J.: Marine ice-cliff instability modeling shows mixed-mode ice-cliff failure and yields calving rate parameterization, Nat. Commun., 12, https://doi.org/10.1038/s41467-021-23070-7, 2021.

450 Crouch, S. L. and Starfield, A. M.: Boundary Elements Methods in Solid Mechanics, Allen Unwin, London, 1983.

Fastook, J. and Schmidt, W.: Finite Element Analysis of Calving From Ice Fronts, Annals of Glaciology, 3, 103–106, 1982.

Freund, L. B.: Dynamic Fracture Mechanics, Cambridge University Press, 1990.

Haseloff, M. and Sergienko, O.: The Effect of Buttressing on Grounding Line Dynamics, Journal of Glaciology, 64, 417–431, 2018.

Krug, J., Weiss, J., O., G., and Durand, G.: Combining Damage and Fracture Mechanics to Model Calving, The Cryosphere, 8, 2101–2117,

455 2014.

Lai, C., Kingslake, J., Wearing, M., Chen, P., Gentine, P., Li, H., Spergel, J., and Wessem, J.: Vulnerability of Antarctica's Ice Shelves to Meltwater-driven Fracture, Journal of Nature, 584, 574–578, 2020.

Nick, F. M., van der Veen, C. J., Vieli, A., and Benn, D.: A Physically Based Calving Model Applied to Marine Outlet Glaciers and Implications for the Glacier Dynamics, Journal of Glaciology, 56, 781–794, 2010.

460 Nick, F. M., Vieli, A., Andersen, M. L., Joughin, I., Payne, A., Edwards, T. L., Pattyn, F., and 20 van de Wal, R. S.: Future sea-level rise from Greenland main outlet glaciers in a warming climate, Nature, 497, 235–238, 2013.

Nye, J. F.: Comments on Dr. Loeweś letter and notes on crevasses, Journal of Glaciology, 2, 512–514, 1955.

Olinger, S. D., Lipovsky, B. P., Denolle, M. A., and Crowell, B. W.: Tracking the Cracking: A Holistic Analysis of Rapid Ice Shelf Fracture Using Seismology, Geodesy, and Satellite Imagery on the Pine Island Glacier Ice Shelf, West Antarctica, Geophysical Research Letters,

465 49, e2021GL097 604, https://doi.org/10.1029/2021GL097604, 2022.

Schoof, C., Davis, A. D., and Popa, T. V.: Boundary Layer Models for Calving Marine Outlet Glaciers, The Cryosphere, 11, 2283–2303, 2017.

Strogatz, S. H.: Nonlinear Dynamics And Chaos, Perseus Books, 1994.

Tada, H., Paris, P., and Irwin, G.: The Stress Analysis of Cracks Handbook, ASME Press, 2000.

470 Todd, J. and Christoffersen, p.: Are Seasonal Calving Dynamics Forced by Buttressing from Ice meĺange or Undercutting by Melting? Outcomes from Full-Stokes Simulations of Store Glacier, West Greenland, The Cryosphere, 8, 2353– 2365, 2014.

van der Veen, C. J.: Fracture Mechanics Approach to Penetration of Surface Crevasses on Glacier, Journal of Cold Regions Science and Technology, 27, 31–47, 1998a.

van der Veen, C. J.: Fracture Mechanics Approach to Penetration of Bottom Crevasses on Glaciers, Journal of Cold Regions Science and
475   Technology, 27, 213–223, 1998b.

Weertman, J.: Can a Water-Filled Crevasse Reach the Bottom Surfaces of a Glacier?, International Association of Scientific Hydrology, 95,
139–145, 1973.

Weertman, J.: Bottom Crevasses, Journal of Glaciology, 25, 185–188, 1980.

Yao, T., Wang, Y., Liu, S., Pu, J., Shen, Y., and Lu, A.: Recent glacial retreat in High Asia in China and its impact on water resource in
480   Northwest China, Science in China Series D: Earth Sciences, 47, 1065–1075, https://doi.org/10.1360/03yd0256, 2004.

Zarrinderakht, M., Schoof, C., and Peirce, A.: The Effect of Hydrology and Crevasse Wall Contact on Calving, The Cryosphere, 16, 4491–
4512, https://doi.org/10.5194/tc-16-4491-2022, 2022.

Zarrinderakht, M., Schoof, C., and Zwinger, T.: A Leading-order Viscoelastic Model for Crevasse Propagation and Calving in Ice Shelves,
The Cryosphere, submitted .

485 Zehnder, A. T.: Fracture Mechanics, vol. 62, Springer London Dordrecht Heidelberg New York, 2012.